RESEARCH PAPER

A Robot-Assisted Microscopy System for Digital Image Correlation in Fatigue Crack Growth Testing

F. Paysan[1] · E. Dietrich[1] · E. Breitbarth[1]

Abstract

Background Digital image correlation (DIC) with microscopes has become an important experimental tool in fracture mechanics to study local effects such as the plastic zone, crack closure, crack deflection or crack branching. High-resolution light microscopes provide 2D images but the field of view is limited to a small area and very sensitive to its alignment. A flexible positioning system is therefore needed to collect such DIC data during the entire fatigue crack growth process.

Objective We present in our paper a new experimental setup for local high-resolution 2D DIC measurements at any location and at any time during fatigue crack growth experiments with a non-fixed DIC microscopy system.

Methods We use a robot to move the 2D DIC microscope to any location on the surface of the specimen. Optical and tactile methods automatically adjust the system and ensure highest image quality as well as accurate alignment. In addition, an advanced repositioning method reduces out-of-plane motion effects.

Results The robot is able to achieve a repositioning accuracy of less than 0.06 mm in vector space, resulting in very low Von Mises strain scattering of 0.07 to 0.09% in the DIC evaluation. The system minimizes systematic errors caused by translation and rotational deviations. Effects such as crack deflection, crack branching or the plastic zone of a fatigue crack can be investigated with a field of view of 10.2 x 6.4 mm^2.

Conclusions The robot supported DIC system generates up to 8000 high-quality DIC images in an experiment that enables the application of digital evaluation algorithms. Redundant information create confidence in the results as all revealed effects are comprehensible. This increases the information content of a single fatigue crack growth test and accelerates knowledge generation.

Introduction

In the century of digitization, Digital Image Correlation (DIC) is a state-of-the-art method in experimental solid mechanics [1]. A contactless optical camera system takes images of a region of interest (*ROI*) and an evaluation software computes full-field displacement and strain data. For this purpose, a reference image of the *ROI* with a speckle pattern is taken and compared with an image of the same *ROI* later [2].

High-resolution DIC is an important tool with increasing robustness for analysing fatigue crack propagation [3–11].

Tong et al. [4, 5] used the local displacement fields to study crack closure in fatigue crack propagation experiments by analysing crack opening displacements (COD) along the crack path. Similarly, Casperson et al. [3] investigated the crack closure behaviour in high-temperature environments. Following their investigations, Vasco-Olmo et al. [6] evaluated shielding effects by crack tip opening displacement measurements (CTOD). Recently, Duan et al. [12] pointed out that COD is strongly dependent on the measurement location in the displacement field and that the crack opening load differs at different locations near to the crack tip. To solve this problem, they introduced the crack opening ratio parameter. Furthermore, Vasco-Olmo et al. [10, 11] used DIC at microscopic level to assess the size and shape characteristics of the plastic zone and related them to crack tip shielding effects. Lu et al. [8], Tong et al. [9] and Carrol et al. [7] investigated the strain and damage accumulation

✉ F. Paysan
 florian.paysan@dlr.de

1 German Aerospace Center (DLR), Institute of Materials Research, Linder Hoehe, 51147 Cologne, Germany

in front of the crack tip. Almost all quantitative evaluations require accurate information about the crack tip position. Réthoré introduced a crack detection algorithm based on a truncated Williams' series [13]. Trained machine learning models determine the crack tip position even in scattered DIC data [14, 15]. The crack tip field can be quantified by the J-integral, stress intensity factors or higher order Williams' series coefficients using energy release integrals J [16, 17], the interaction integral [18, 19] or the near field itself [20]. A more recent technique for quantifying crack tip loads is the CJP model [21].

However, most experimental investigations of the plastic zone use a fixed camera setting and are therefore limited to a small *ROI* [22, 23]. Only effects occurring in this specific *ROI* can be captured. Consistent data along the entire crack path promise great potential for a better understanding of fatigue cracks [24, 25]. Liang et al. [26] identified this issue and used a non-fixed camera system for capturing DIC images. They concluded, that DIC error sources in such systems are a considerable challenge. Because of the high magnification of optical light microscopes [27], the two-dimensional DIC evaluation is sensitive to external influences. Zhao et al. [1] summarized the potential sources of errors affecting the two-dimensional DIC measurements as follows:

- *Quality of speckle pattern*
- *Image quality (contrast, sharpness)*
- *Test environment conditions*
- *Out-of-plane motion*

The choice of the DIC facet size depends strongly on the quality of the speckle pattern [28–31]. Dong et al. [31] summarized that a good speckle pattern should have high contrast, randomness, isotropy and stability. Contrast deficits and image blurring pose a significant problem in identifying the required features within a facet. The pattern distribution should be non-periodic and non-directional. Furthermore, the speckle pattern should deform together with the specimen surface. Different methods for assessing the speckle pattern quality have been developed by Lecompte et al. [29], and Liu et al. [30] using image morphology. Liu et al. [30] introduced the Shannon entropy and concluded that the pattern quality increases with this parameter. Crammond et al. [28] examined the influence of speckle size and density within a facet. A higher density of significant features reduces scatter and provides more accurate results. Pan et al.[32] and Dufour et al. [33] investigated the effect of lens distortion on the accuracy of DIC. They concluded that the deviations are small and can be neglected if no large deformation gradients are expected in the distorted areas. Quian et al. [27] pointed out that lens distortion has a significant error impact in combination with rigid-body motion in DIC microscopy due to

the change of blurriness of features within a facet. The influence of the test environment affects the DIC measurement mainly through changes in *ROI* exposure or a moving target caused by vibrations. While a variation in exposure results in a change of the recognized features within a facet [28, 29], moving targets lead to rigid-body movements. Zappa et al. [34] pointed out that a moving target in dynamic systems consequences a blurring effect on the acquired images. Sutton et al. [35] investigated the influence of translational and rotational deviations on the 2d DIC evaluation and Hoult et al. [36] concluded that out-of-plane movements are the most elementary source of error in two-dimensional DIC evaluations. In particular, deviations in the distance between camera and surface as well as incorrect alignment angles must be minimised. Haddadi et al. [37] suggest to first identify all possible out-of-plane movement sources to reduce scattering. Zhang et al. [38] described the influence via a change in the mapping between pixel and detected feature. Finally, Zhao et al. [1] and Pan et al. [39] concluded that all those potential error sources strongly depend on the experimental set-up. Additionally, the total DIC error is always a combination of the possible error types mentioned above, which makes it very difficult to subsequently separate and correct the individual errors.

Our paper addresses this gap for non-fixed high-resolution DIC system by presenting a new experimental mechanical testing system that uses multiscale DIC to generate autonomously a large amount of data. In contrast to current research, we use a non-fixed 2D DIC microscope system mounted on a robot. This enables moving to different locations at the surface of the specimen and to capture specific *ROI* during fatigue crack growth. In combination with advanced automatic focussing algorithms, we can reduce potential DIC error sources, mentioned above. As a result, this system can capture temporally and spatially resolved local displacement fields along the entire fatigue crack growth. Thus, fatigue crack growth mechanisms such as crack branching, deflection, crack closure and the plastic zone can be investigated at a very detailed level.

Methodology

Advanced Test Stand

In order to capture local effects of the crack tip field, high-resolution displacement data near the crack tip location at any time of fatigue crack growth is required. Figure 1(a) shows our experimental setup. All fatigue crack propagation experiments are in accordance with ASTM E647-15 [40].

The basis of the setup is a servo-hydraulic uniaxial testing machine with a 2-mm-thick MT(160) sheet specimen. The specimen used is made of the aluminium alloy AA2024-T3.
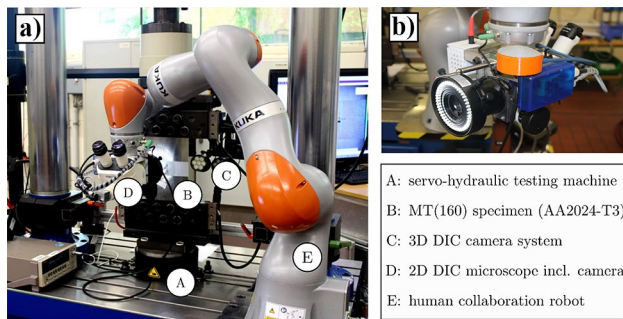
Fig. 1 General test setup: (**a**) overview and (**b**) the 2D DIC microscope including camera, light source and inspection probe

The rolling direction of the sheet is perpendicular to the crack propagation direction. In this example, the specimen is subjected to a uniaxial sinusoidal load with constant amplitude. The maximum nominal load is $F_{max} = 15$ kN with a load ratio of $R = 0.1$ and a test frequency of $f_{cycle} = 20$ Hz. The test is supplemented by a direct current potential drop (DCPD) system ($I_{DC\text{-}POT} = 100$ A = const., $U_{DC\text{-}POT} = 60$mV) for crack length measurement. Here, the voltage drop is measured at two pins 10 mm below and above the initial saw notch, respectively. Two multi-scale DIC systems are the core of the test stand. A GOM Aramis 12M 3D DIC system at the rear of the test stand captures displacement data of the entire specimen surface.

The 3D DIC system consists of two single 12 Megapixel cameras (4619 x 2598 pixels) with a slider distance of 98 mm and an angle of 25° to each other. The measurement volume is set to 200 x 150 x 21 mm³ and 50 mm lenses are used. The distance to the specimen surface is 525 mm. Two external lamps (power = 20 W, beam angle = 19°), included in the GOM Aramis system, are used as the light source to achieve a uniform illumination of the specimen surface. For DIC evaluation, the back side of the specimen is primed with white varnish and afterwards a fine random black dot pattern is sprayed, to ensure pattern stability and to provide maximum contrast for feature identification. Here, a facet size of 19 x 19 pixel (0.86 mm x 0.86 mm) in combination with a facet distance of 16 pixel (0.59 mm x 0.59 mm) is used. The new microscopic 2D DIC (MDIC) system is located on the front side of the specimen. It consists of an optical Zeiss 206C stereo light microscope, including a Basler a2A5320-23umPro global shutter 16 Megapixel CMOS camera (5333 x 3000 pixels) and a straight inspection probe (see Fig. 1(b)). The KUKA LBR iiwa 14 R820 cobot carries the DIC microscope. A ring light (power = 9 W) is used for illumination (see Fig. 1(b)) and an exposure time of 200 ms ensures a good contrast for feature identification. This allows the DIC microscope to be positioned on any location on the specimen surface. At a magnification of 1.6x, the facet distance is 0.047 mm (facet size: 40 x 40 pixel, facet
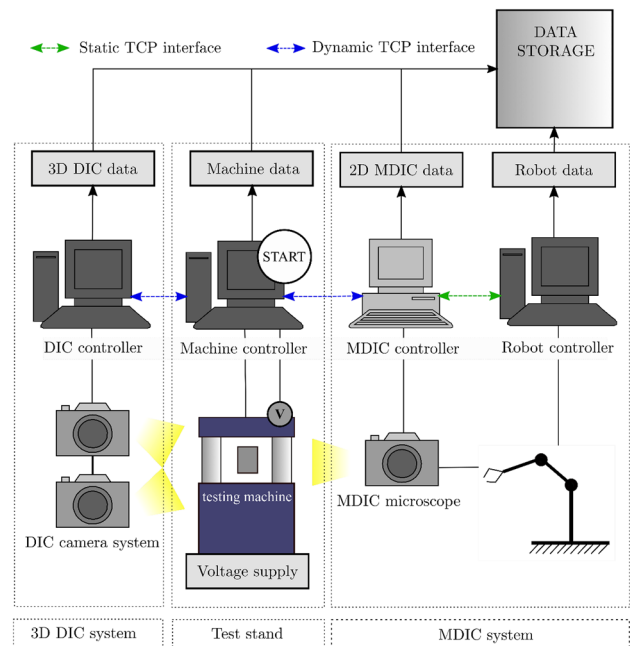

Fig. 2 Schematic structure of the testing system including the DIC measurement systems and their Ethernet communication structure

distance: 30 x 30 pixel). With the used magnification, the field of view of the microscope is 10.2 mm x 6.4 mm. For the MDIC evaluation, the front of the specimen is coated with white paint and then sprayed with a mixture of black iron oxide powder and liquid ethanol using an airbrush (1.8 mm nozzle, 2.4 bar spray pressure).

A schematic representation of the experimental setup is given in Fig. 2. The MTS FlexTest 40 Controller together with the MTS TestSuite Multipurpose Elite Software controls the servo-hydraulic testing machine and communicates with the DIC systems. This system focuses safety aspects, and therefore the testing machine is mainly responsible for the whole test sequence. The test program is based on the Multipurpose Elite software and is extended by custom made Python communication scripts. The machine controller triggers the external 3D DIC and the 2D MDIC system via Ethernet communication. For this purpose, temporal dynamic Transmission Control Protocol (TCP) interfaces are opened, which send the corresponding trigger signal. In addition to the action command, it contains further machine data, such as the number of load cycles, current force and displacement. The TCP interface remains open until the requested action is completed by a response message from the corresponding DIC system. This prevents the test sequence from continuing in the event of an error within the DIC acquisition systems.

If the 3D-DIC system is activated by a command over the TCP stream, an image is captured and all metadata listed in the Table 1 are additionally stored. This image metadata makes the entire test reproducible and thus allows

Table 1 Sources of data and their information stored during the test procedure

Data source	Stored information
Machine data	Force, displacement, frequency, crack length via potential drop, load cycles, time
2D MDIC data	Raw MDIC images, exposure time, image quality parameters
Robot data	Desired coordinates, actual coordinates, current axis angles
3D DIC data	Raw DIC images, exposure information

comparisons between all other types of measurement data. Then, the MDIC system is also activated via a corresponding TCP command. In general, the MDIC system consists of the MDIC controller, the robot controller, the robot arm and the MDIC microscope. When the MDIC controller receives a trigger signal, it submits the coordinates to the robot controller, which commands the robot arm to guide the microscope to the desired position. If this is successful, an image is captured and the corresponding metadata is stored. The process is repeated until all the desired positions are covered.

In total, a single crack propagation experiment produces up to 8000 individual images with a data volume of about 350 GB. To obtain full-field displacement information of the specimen surface, the raw images are processed using the GOM Aramis 2020 software. When the test is finished, all remaining TCP interfaces are closed.

Test Procedure

In general, the test procedure consists of two phases, as shown in Fig. 3. The DIC calibration takes place before the actual test. Then, the DIC data acquisition phase coordinates the image acquisition during fatigue crack growth.

Figure 4 gives an overview of the activities done by the 2D MDIC system during calibration and measurement phase. Before starting a test, the specimen is completely unloaded to obtain a reference DC potential at zero load needed for the crack length measurement. For this purpose, the machine records a data set over a period of 10 s with a sampling rate of 254 Hz and the average value recorded is used as reference. During the test, the DCPD crack length
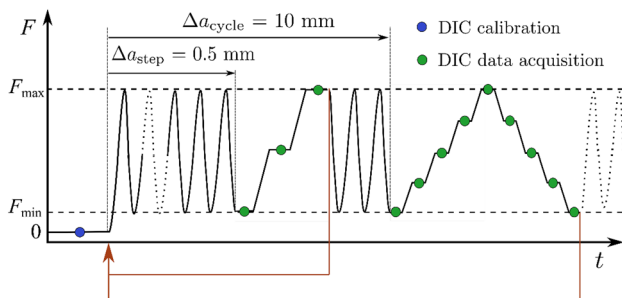
controls all further steps [40]. The influence of local effects such as crack deflection or crack branching can be neglected as their scale (< 0.5 mm) is significantly smaller than the macroscopic mode I fatigue crack. During calibration the robot starts moving to four points at the specimen surface and touches them by using a straight inspection probe (Fig. 1(b)). With the received coordinates, a working plane aligned and centred with the surface is computed and set as a new base coordinate system. For more detailed information, see "Alignment of the Base Coordinate System". Then two points are approached at x,y = [30,0], [-30,0] and the system checks if the microscope's line of sight is exactly perpendicular to the specimen surface. For this purpose, we developed a new optical cluster algorithm that uses the characteristic focus point of a captured image. Both aligning methods together take about 3 min. If this condition is not satisfied, the base coordinate system will be adapted. In the following, the user inputs an area in which the crack probably will grow as given in Fig. 4.
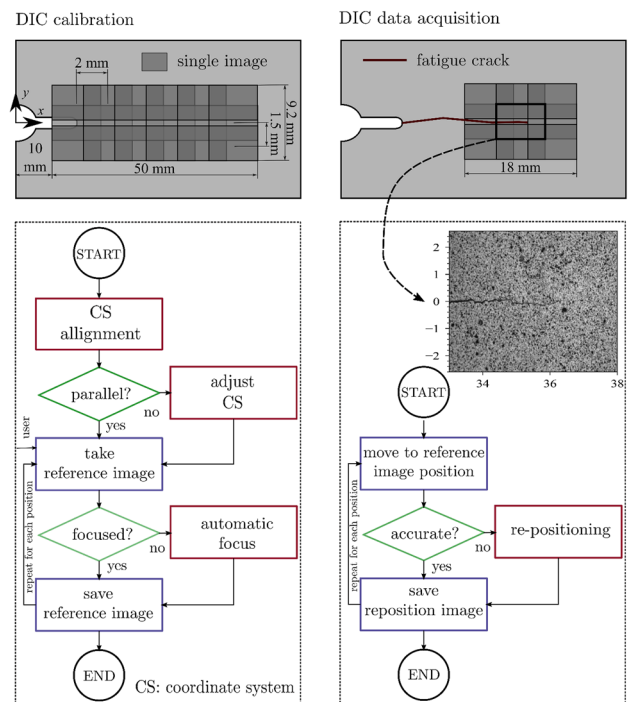

Fig. 3 Testing procedure with DIC image acquisition trigger points

Fig. 4 MDIC system activities during calibration and measurement phase

The robot then moves the MDIC microscope in a checkerboard pattern to capture reference images with 70% overlap in the defined region. At each location, the sharpness of the image is checked and adjusted according to the sharpness index presented in "Image Focusing". If the sharpness does not meet a certain limit, the depth is adapted by the robot until the images are focused. Thus, taking one single reference image can take up to 1 min until all quality conditions have been satisfied. Finally, the reference image is taken and all metadata are stored as listed in Table 1. The actual position of the reference images is particularly important here. This procedure is repeated for each location within the defined domain. Angle and focus checks are performed to ensure highest image quality and to avoid incorrect displacement measurements due to misalignment between the MDIC system and the specimen surface.

After the calibration phase, the measurement phase takes place. Here the specimen is loaded cyclically with a constant amplitude until a crack propagation increment of $\Delta a_{step} = 0.5$ mm is measured by DCPD. Then, the load sequence is stopped and three different load levels are approached: minimum, intermediate and maximum load. At each load level, the 3D DIC system is triggered first and then the 2D MDIC system. The robot moves the MDIC microscope to the locations of the reference images in the proximity to the estimated crack tip. The approximated position of the crack tip is determined with the DCPD method $x_{ct}, y_{ct} = a, 0$. When the robot moves to a reference image position, the re-position accuracy and the re-position misorientation angle is checked and if it is below a user-defined values of $x_{abs} = 0.06$ mm and $\Phi_{abs} = 0.015°$ (see "Dynamic DIC Scattering"). These values are a suitable trade-off between DIC quality and repositioning accuracy. Otherwise, repositioning to the desired coordinates is repeated until the threshold values are reached. A direct correction of the measured position errors is not possible, as the robot is not able to perform such small movements with sufficient accuracy. We define the reposition accuracy as the absolute distance in vector space between the desired reference image position and the actual position. If this condition is satisfied, the image for the current stage is stored. The machine controller repeats this process until the specimen finally breaks.

Alignment of the Base Coordinate System

Aligning the optical system to the measurement plane is an important task when setting up a 2D DIC system. Misalignments have a significant impact on the DIC scattering and cause spurious displacements. To ensure vertical alignment of the camera's line of sight to the specimen surface, the robot defines a new working plane. Therefore, it touches the surface of the specimen with an inspection probe at four different locations (see Fig. 5). Contact is detected as soon as the measured force exceeds 10 N. Based on these coordinates relative to the origin coordinate system, the new base coordinate system is computed:

The initial distance between the head of the inspection probe and the specimen surface l is 167 mm in the depth direction. Based on the measured distances of the touching points, the system is able to determine the rotation angles α_{cs} and β_{cs} by

$$\alpha_{cs} = \sin^{-1}\left(\frac{f[\text{mm}]}{50\text{mm}}\right) \tag{1}$$

$$\beta_{cs} = \sin^{-1}\left(\frac{g[\text{mm}]}{30\text{mm}}\right) \tag{2}$$

Following, based on those angles the systems spans a virtual plane which is parallel to the specimen surface. This plane serves as basis for all further movements of the robot and microscope.

Image Focusing

The image focusing algorithm is required for both parallelism checking and image focusing in the calibration phase. This algorithm ensures good image quality in terms of contrast and sharpness, which is essential for a high-quality DIC evaluation. The method is explained with an example speckle image (see Fig. 6(a)) captured with the MDIC system. The grayscale image contains pixel values from 0 to 255. The general approach is that good image sharpness is characterized by large gradients between dark (I = 0) and white (I = 255) pixel areas.

Therefore, the image is derived twice by applying a Laplacian transformation (see Fig. 6(b)) as given in the following formula. The repeated derivation is performed in order to weight the importance of image gradients once more.
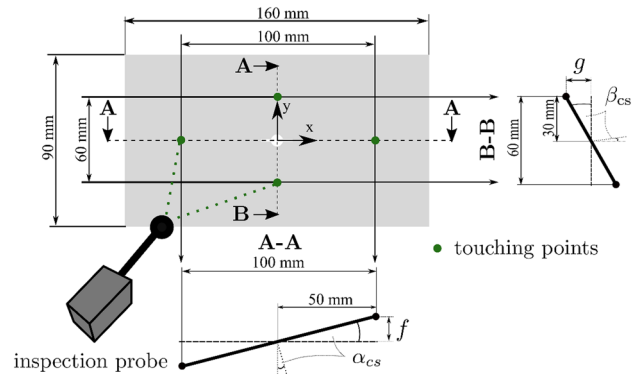

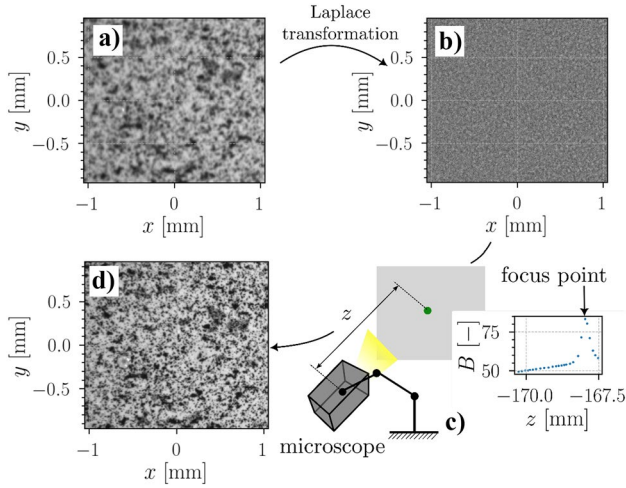**Fig. 5** Aligning base coordinate system relative to the specimen surface by four-point touching

Fig. 6 (**a**) speckle pattern image, (**b**) Laplacian-transformed image, (**c**) its distribution and (**d**) depth-of-field

Fig. 7 Adjusting the alignment of the microscope by evaluating the focus point

$$\nabla^2 I = \frac{\delta I^2}{\delta x^2} + \frac{\delta I^2}{\delta y^2} \tag{3}$$

Figure 6(b) shows the Laplacian-transformed image. Only the edges of the speckle pattern are still visible. In this example, these edges are more pronounced in a focused area of the image. In Fig. 6(c), the histogram of the Laplacian-transformed image follows a Gaussian normal distribution with mean $\mu(\nabla^2(I)) \to 0$. We use the variance $V(\nabla^2(I))$ as a sharpness indicator. However, this indicator strongly depends on the quality of the speckle pattern, exposure, or contrast. For example, large speckles reduce the maximum variance in contrast to a large number of small speckles. Low exposure or contrast smooths the transition between the speckles and its background, which results in lower gradients. Since the speckle pattern on the microscope side is generated by airbrush, it can have locally different properties. Therefore, the achievable sharpness index $B = V(\nabla^2(I))$ differs locally and must be determined individually.

To do this, the robot moves the MDIC system continuously in an interval of $z = [-1, 1]$ mm in depth direction. Every $\Delta z = 0.05$ mm, an image is captured and its sharpness index B is calculated. This results in a curve describing the sharpness as a function of depth z, as shown in Fig. 6(c). The location of the maximum value defines the focus point and the maximum value itself serves as sharpness reference index B_b, which is used to check the sharpness. Then, the robot moves the MDIC system again in the mentioned interval back to the noticed focus point until the sharpness index limit B_b is reached. The image taken after applying the presented focus algorithm is given in Fig. 6(d).

With the focus algorithm, we additionally ensure that the view direction of the MDIC system is completely vertical to th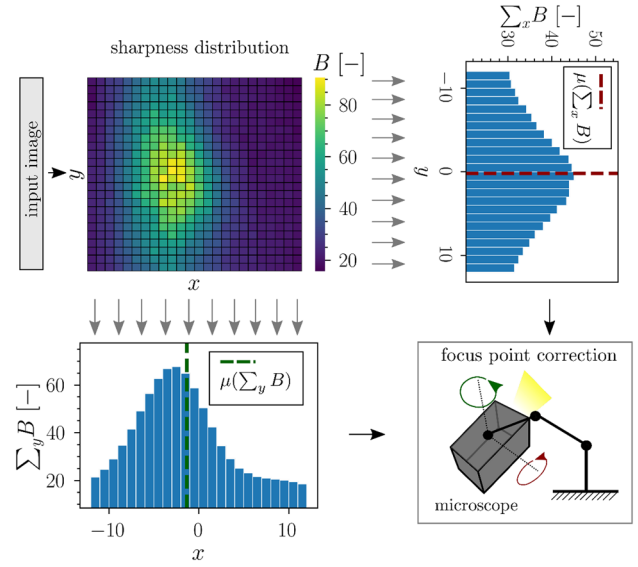e specimen surface. Therefore, the image is divided into 25x25 sub-regions and their sharpness index B is determined, resulting in the focal heatmap shown in Fig. 7. In general, the number of sub-regions is a user-defined value and depends on the density of the speckle points. We choose 25x25 sub-regions so that there are several black and white speckles in each region (approx. 10 to 20). This allows stable application of the focus algorithm and the determination of B. In addition, we do not use a telecentric lens to apply DIC as we use the inherent distortion of the lens to achieve a perfect alignment. In 7 out of 8 cases, this procedure is not necessary because the alignment by the touching points procedure is adequate. However, in rare cases, the alignment is not satisfactory due to the positioning error of the robot. The following algorithm solves the problem:

The sharpness indices B of all sub-region are summed up for each row and column in horizontal and vertical direction. The distribution of the mean values $\mu(\sum_{x,y} B)$ describes the position of the focus point in the x or y location at the maximum value $x_{max}(\mu(\sum_y B))$ and $y_{max}(\mu(\sum_x B))$. In this example, the mean value $y_{max}(\mu(\sum_x B)) = 0.048$ is smaller than 0.1 and no correction in needed. To determine the threshold value of 0.1, we applied the algorithm 15 times in a row to the same misaligned surface and examined the lowest achievable value. We found, that 0.1 is the lowest deviation that can be achieved with this algorithm and can be associated with the actual misalignment of the camera system. Optical alignment values less below 0.1 are often due to local artefacts in the speckle pattern rather than actual misalignment. In contrast, the x-direction is off-centre with $x_{max}(\mu(\sum_y B)) = -1.124$ and therefore, the viewing directions is not perfectly vertical to the specimen surface. The new rotation angles are calculated according to the following formulas:

$$\alpha_{cs} = C_x * x_{max}(\mu(\sum_y B)) \tag{4}$$

$$\beta_{cs} = C_y * y_{max}(\mu(\sum_x B)) \tag{5}$$

These formulas result from a parameter study performed by the robot, where the rotation angles α_{cs}, β_{cs} are varied. The results showed that there is a linear relationship between the angles and the optical algorithm output $x_{max}(\mu(\sum_y B))$ and $y_{max}(\mu(\sum_x B))$, respectively. However, this linear relationship is highly dependent on the chosen magnification of the microscope. For the chosen magnification of 1.6x, we identified $C_x = C_y = 0.5$ to be the best for our setup.

If a misalignment is detected, the correction procedure is repeated in a loop until the 0.1 threshold, explained above, is reached. Speckle pattern artefacts are also visible in the focus heatmap, but the algorithm is not sensitive to them. Furthermore, with the help of this algorithm we found out that the microscope's viewing direction is not exactly concentric with the lens, but shifted by 5°. If misalignment is detected by the optical algorithm, it usually takes 1-3 iterations of the presented method to correct the alignment. The whole procedure can take up to 30 s.

Results

For evaluating the quality of the microscopic DIC data, we analyse exemplarily the displacements and von Mises strains of a fatigue crack with a total length of $a = 28$ mm and compare them with finite element (FE) simulations as shown in Fig. 8(a). All measuring points are located about 2 mm above the fatigue crack and have a horizontal distance of 1 mm from each other. The specified vertical distance from the fatigue crack was chosen to reduce the impacts of local effects such as crack branching or deflection, which often lead to local strain gradients near the crack edges. This means that the determined strains of the measuring points should mainly result from the loading conditions and the elasticity properties of the material.

In order to receive reference strains, we perform a fatigue crack FE simulation with exactly the same boundary and loading conditions as applied in the experiment (see "Test Procedure"). A detailed description of the finite element model, meshing strategies, material model and definition of boundary conditions is given in [41]. In summary, we performed a 3D crack propagation FE simulation of an MT160 model based on the releasing-constraint crack propagation algorithm. The material model is based on bilinear isotropic hardening to approximate the material behaviour of AA2024-T3. Extracting the nodal strain solution from the surface serves as reference for assessing the quality of the microscopic DIC measurement performed.
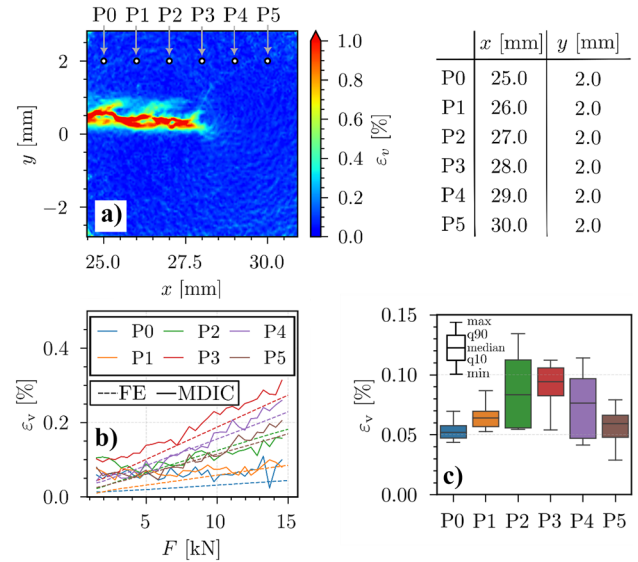

Fig. 8 (**a**) definition of measurement points in a full-field strain field containing a fatigue crack of a length of a=28mm, (**b**) analysis of the point strain in dependency of the load and (**c**) analysis of measuring the same point in eight different DIC images

Figure 8(b) shows the obtained strains from both methods as a function of the load. In general, the curves obtained from the DIC data show good agreement with the strain solution from the FE simulation. P0 shows the lowest DIC strain gradient while P3 is characterized by the largest increasement of strain accumulation during a loading or crack opening, respectively, sequence. However, it is noticeable that especially in the beginning at low loads from 1.5 kN to 5 kN the results based on DIC differs from the FE data. All curves show higher values than it is expected from FE results. The largest difference between FE solution and strains obtained from DIC is given by P3. The point P3 is located exactly above the crack tip position. Furthermore, significant differences between FE and DIC can be observed at P4 and P5. While for medium loads (from 5 kN to 10 kN) both points match very well, the strains based on DIC increase more steeply at loads larger than 10 kN. From "Conclusion" and Fig. 4, respectively, we know that displacements of a certain point are measured multiple times due to the 70% overlap of the images taken in a checkerboard pattern. In detail, displacements of points located at $y = 0$ mm can be determined from eight different images. This leads to a high redundancy of the measured DIC data. Figure 8c illustrates the statistical evaluation of the measured von Mises strain each point but from eight different images. All images are taken at minimum load of 1.5kN. By studying Fig. 8(c), we can identify that the median values of strains near to the crack tip position tends to be approximately 1.5 times larger than at larger distances behind or in front of the crack tip. The strains determined from points behind the crack tip (P0

and P1) have a low inherent scatter. In fact, at both points the measured strain values differ in a range from max. +0.03% to min. -0.01% related to the respective median. The points near the crack tip have the largest scatter. Especially, the points P2 and P4 have strain ranges from +0.06% to -0.03%. In summary, the results show that the strains for all images have a scatter lower than 0.1%.

Discussion

The discussion aims to separate the individual effects that are responsible for the characteristics shown in the "Result". Here, we distinguish between static and dynamic scattering effects. Static scattering mostly results from inherent influences of the DIC setup on the results. As dynamic scattering effects we declare all scattering causes that are directly related to the movement of the robot, e.g. out-of-plane movement. Furthermore, we choose the von Mises strain as scattering indicator since all components of the strain tensor are included.

Static DIC Scattering

The static DIC analysis reveals the scatter of a DIC evaluation caused by inherent imaging errors and environmental conditions like the CMOS sensor noise, illumination, temperature convection, air movement or vibrations. For this purpose, several images with identical setup are taken under the same conditions at zero load. The DIC evaluation is performed with a facet size of 40 x 40 pixels (0.063 mm x 0.063 mm) and a facet distance of 30 pixels (0.047 mm). Each facet encloses at least two significant features of the black and white pattern. It is important that there is no movement between the images in this analysis. Therefore, errors due to out-of-plane motion are negligible. Figure 9(a) shows the von Mises strain field based on two images taken.

Qualitatively, the von Mises strain field in the centre region is characterized by a low inherent scatter in a range from ε_v 0.01% to 0.05%. This scatter can be associated to environmental reasons, such as flickering in exposure, sensor scatter or very small vibrations of the testing system. Nevertheless, the strains at the edges of the strain field plot are about twice as large as in the centre. Furthermore, local artefacts are visible in the lower right corner of the evaluated field (red spots with von Mises strain > 0.20%). Those artefacts can be related to bad pattern quality. That means pattern regions with a low number of features, e.g. in case of too big pattern points or a small number of single pattern points, lead to miscalculations of the corresponding displacements. Interestingly, there is another artefact located in the centre region at x, y = [-0.7, -1.4]
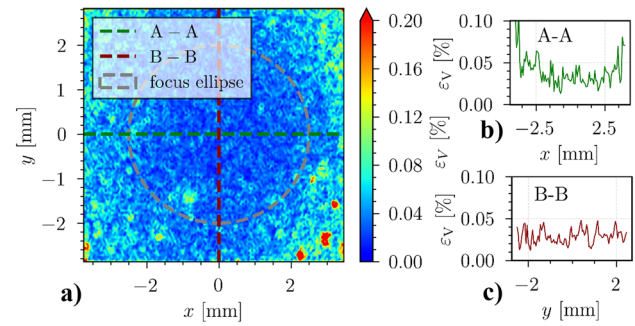

Fig. 9 (**a**) von Mises strain field at zero load of a static DIC evaluation without motion between image capture and the absolute strain values of a (**b**) horizontal and (**c**) vertical path

which also results from bad pattern quality. Comparing the maximum strain values of artefacts in both locations, we observe that the strain values of the artefacts located near the edges are twice as large. This effect is associated to the lens distortion of the microscope. The distortion leads to a stronger scatter up to a maximum von Mises strain of 0.15%, but amplifies the effect of local pattern artefacts. The distortions lead to a loss of image sharpness which makes it difficult to identify the features needed for the DIC evaluation.

Therefore, we focus our evaluations on the centre of the image, which is not as affected by lens distortion. The von Mises strain values of path A-A (see Fig. 9(b)) reveal that the focused area extents from x = -2.5 mm to x = +2.5 mm. On path B-B (see Fig. 9(c)), we decide on a focused region between y = -2 mm and y = +2 mm. Based on those values, the focus ellipse is defined by:

$$\frac{x^2}{2.5\text{mm}} + \frac{y^2}{2.0\text{mm}} = 1 \tag{6}$$

Within this ellipse, the inherent scattering of the DIC evaluation can be considered lower than the median value of the total strain field. This means that we expect scattering von Mises strains up to maximum of 0.05 %.

For statistical reasons, ten of those DIC evaluations, described above, have been performed and analysed regarding their scatter. The results in Fig. 10, show a constant median of 0.43 % von Mises strain along all DIC evaluations performed. Only the maximum value differs slightly from 0.11 % to 0.13 %.

Dynamic DIC Scattering

DIC errors in a 2D setup with a moveable camera are mainly caused by misalignments, i.e. out-of-plane motions, to the position of the reference image. Here, the repositioning accuracy of the robot is the most important factor. The deviation
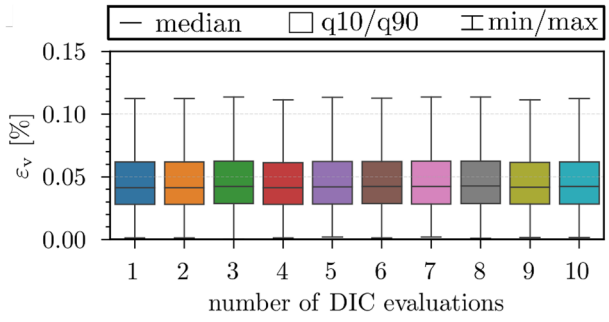
Fig. 10 Analysis of the static DIC scatter of ten different DIC evaluations without robot movement

Fig. 11 Von Mises strain field of a DIC evaluation after two repositioning runs with $x_{abs} = 0.055\,mm$ and $\phi_{abs} = 0.0135°$

between the position of the reference image and the position of the repositioning image is described as follows:

$$x_{abs} = \sqrt{\left(x_{rep} - x_{ref}\right)^2 + \left(y_{rep} - y_{ref}\right)^2 + \left(z_{rep} - z_{ref}\right)^2} \quad (7)$$

Here x_{ref}, y_{ref}, z_{ref} are coordinates of the reference image and x_{rep}, y_{rep}, z_{rep} are the position after repositioning in the DIC measurement phase. Next to the translational degrees of freedom, misalignments can occur in the rotational axis, too. Here, we define an equivalent angle of rotation that is described as follows:

$$\phi_{abs} = \sqrt{\left(A_{R,rep} - A_{R,ref}\right)^2 + \left(B_{R,rep} - B_{R,ref}\right)^2 + \left(C_{R,rep} - C_{R,ref}\right)^2} \quad (8)$$

In this formula, A_R, B_R and C_R define the rotational angles of the corresponding translational axis (x,y and z). In order to assess the influence of the repositioning of the robot, we conducted the following experiment: After surface alignment and automatic focusing (using the algorithms in "Test Procedure") a reference image is taken. Then the robot is moved 20 mm in x-direction, followed by a repositioning process to the origin position. Here, the repositioning accuracy and equivalent angle of rotation are determined by the internal robot position sensors. In our experiment, we approached the same position for different runs and figured out that the measured position is reproduced within a range of +/- 0.01 mm. In total, the repositioning runs were repeated ten times and each captured image was related to the reference image.

Figure 11 shows the von Mises strain field after two repositioning runs. We used the same image position as in the static analysis in Fig. 9(a). The repositioning accuracies are $x_{abs} = 0.055\,mm$ and $\phi_{abs} = 0.0135°$, as can been seen from Fig. 12 (number of DIC evaluation = 2).

In this example, the overall scatter in Fig. 11 increases significantly especially at the corners of the image. But again, we distinguish between the distorted area near the corners and the focused area within the defined focus ellipse. Figure 11 shows that the effect of lens distortions are greater
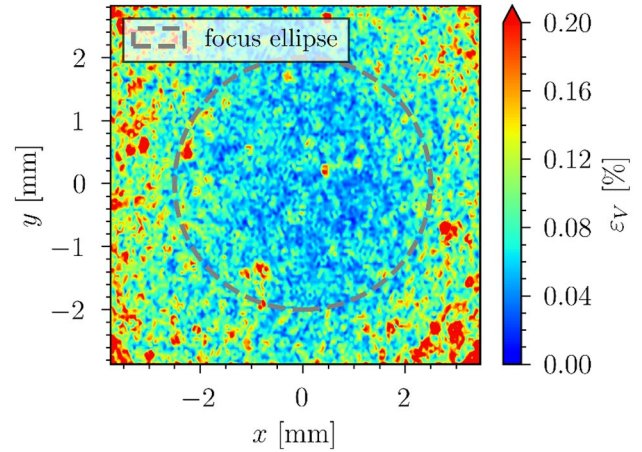
compared to Fig. 9(a). Compared to the static analysis, the local artefacts in lower right area are even more pronounced. All those effects result from an additional loss of image sharpness which can be associated with out-of-plane movements of the robot during the repositioning process.

Figure 12 shows a correlation between the repositioning accuracy x_{abs} and the DIC scatter. In general, the robot achieves the desired position with an accuracy less than 0.1 mm in vector space. All repositioning experiments with a repositioning accuracy lower than 0.035 mm have a median von Mises strain of about 0.057%. In contrast,
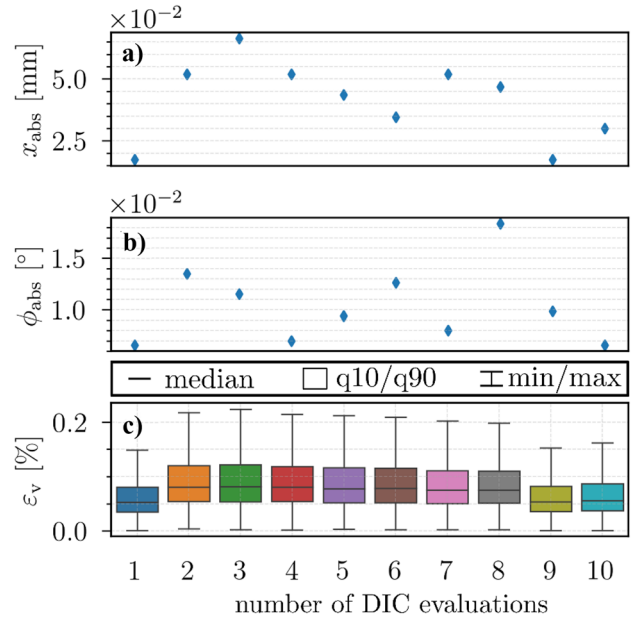

Fig. 12 Dynamic DIC scatter for 10 repositioning experiments: (**a**) the repositioning accuracy x_{abs}, (**b**) the repositioning angle accuracy Φ_{abs}, (**c**) von Mises strain statistics of the DIC evaluation

all other runs have a repositioning accuracy of more than 0.035 mm. Here, the medians in von Mises strain are mainly in a range between 0.079% and 0.082%. To reduce the scatter during the fatigue crack growth test, we have set 0.06 mm as the limit for the repositioning process explained in "Test Procedure".

Additionally, Fig. 12 reveals that the angle of rotation has a smaller influence on the scatter. The DIC evaluation #8 has a large misorientation of 0.0182°, but both the maximum and the median of the von Mises strain are still within the range of all other runs. Nevertheless, the whole system guarantees a very high DIC evaluation quality with an average scatter of less than 0.085 % von Mises strain. Especially small elastic strains can be captured in great detail by the system. The scatter analysis also explains the plateau like behaviour at small loads (from 1.5kN to 5kN) from Fig. 8(b). Here, the scatter becomes dominant and strains smaller than 0.085% can no longer be revealed. We also found that the measured strains at points P4 and P5 increase more steeply at larger loads. This effect can be explained by the lens distortion of the microscope. At larger loads, the speckle points are shifted into the distorted region, resulting in a local amplification of the scatter.

Apart from out-of-plane motion, out-of-plane rotation is one of the main challenges in non-fixed 2D DIC system set-ups, because it leads to spurious gradients in the computed DIC displacements. This systematic error affects the application of path-independent integrals such as the J and interaction integral and should therefore be avoided. Figure 13(a) illustrates displacements u_x along the path A-A in Fig. 9. Except for #8, all curves have the same gradient. No gradient is visible within the focus ellipse any more, but only outside in the distorted areas. The lens distortion supports the effect of small misalignments. Therefore, we strongly recommend to apply further evaluation only within the focus ellipsis. Nevertheless, #8 shows a large gradient in x direction. Sometimes the robot is not able to align the microscope accurate enough,
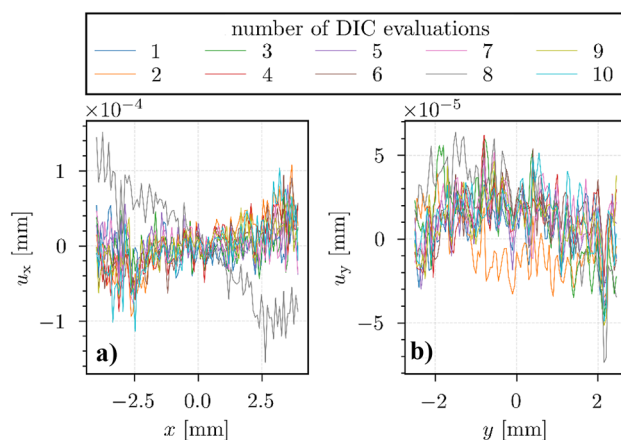
which leads to this kind of systematic errors. Therefore, we defined the maximum misorientation angle to 0.015°. If this angle is exceeded by the robot, another repositioning attempt is performed. Furthermore, the analysis of gradients in vertical direction (path B-B in Fig. 9) reveals that the system is not sensitive to deviations in this direction.

Conclusion

A robot is a great extension in classical mechanical experiments for automated high resolution 2D DIC analysis. Because of the high reposition accuracy, the von Mises strain fields have spurious strains with less than 0.085 %. That makes it possible to investigate strains (greater than 0.1%) close to fatigue cracks to reveal local mechanisms such as crack closure, crack branching or deflection. The ability to obtain both time-resolved data and data from any crack length enables investigations of fatigue cracks at a whole new level. In addition to conventional methods such as post-mortem fracture surface analysis, this method promises high potential for getting a better understanding about cause-and-effect relationships of fatigue crack mechanics. Furthermore, the ability to autonomously generate an enormous amount of high-quality experimental data is a key technology for data-driven methods in experimental mechanics.

In addition, the following conclusion can be made:

1. Robotic arms are able to guide sensitive 2D microscope systems for high-resolution DIC measurements due to their high positioning accuracy of less than 0.1 mm. In addition, multiple repositioning to the desired location enables an increase in accuracy up to 0.048 mm in vector space.
2. Due to their seven degrees of freedom in motion, robotic arms in combination with optical or tactile automated methods can compensate systematic errors in the alignment of the camera to the specimen surface to prevent erroneous displacement or strain mapping in the DIC measurement.
3. Using a microscope in flexible 2D DIC setups is a challenge to retrieve low DIC scattering. The main problem is the lens distortion which is even more pronounced by out-of-plane motion caused by misalignments.
4. In the focused centre region, we can achieve scatter of less than 0.085% von Mises strain. Furthermore, no displacement gradient has been identified in this area which recommends it as basis for further analysis.
5. The robot supported DIC system generates up to 8000 high-quality local DIC images that enables the application of digital evaluation algorithms. Redundant information create confidence in the results as all revealed effects are comprehensible. This increases the information content of a single fatigue crack growth test and accelerates knowledge generation.

Fig. 13 Analysis of the impact of misorientation on DIC displacements

Nomenclature α_{cs} : Coordinate system rotation angle – y axis [°]; a : Crack length [mm]; Δa: Crack length increment [mm]; Δa_{step} : Crack length increment for load level image capture [mm]; Δa_{cycle}: Crack length increment for cycle image capture [mm]; A_R : Rotation angle around x-axis [°]; $A_{R,ref}$: Rotation angle around x-axis of the reference image [°]; $A_{R,rep}$: Rotation angle around x-axis of the reposition image [°]; β_{cs} : Coordinate system rotation angle – x axis [°]; B : Image sharpness indicator [-]; B_b : Image sharpness boundary [-]; B_R : Rotation angle around y-axis [°]; $B_{R,ref}$: Rotation angle around y-axis of the reference image [°]; $B_{R,rep}$: Rotation angle around y-axis of the reposition image [°]; C_R: Rotation angle around z-axis [°]; $C_{R,ref}$: Rotation angle around z-axis of the reference image [°]; $C_{R,rep}$: Rotation angle around z-axis of the reposition image [°]; d_f : Focus distance [mm]; ε_V: Von Mises strain [%]; f_{cycle} : Test frequency [Hz]; f : Surface touching difference distance (horizontal) [mm]; F : Force [kN]; F_{max} : Maximum force [kN]; F_{min} : Minimum force [kN]; g : Surface touching difference distance (vertical) [mm]; I_{DC-Pot} : Current for potential drop measurement [A]; R : Load ratio [-]; U_{DC-Pot} : Voltage for potential drop measurement [V]; x : x-coordinate [mm]; x_{abs} : Reposition accuracy [mm]; x_{ct} : x-coordinate of the crack tip [mm]; x_{ref} : x-coordinate of the reference image [mm]; x_{rep} : x-coordinate of the reposition image [mm]; y : y-coordinate [mm]; y_{ct} : y-coordinate of the crack tip [mm]; y_{ref} : y-coordinate of the reference image [mm]; y_{rep} : y-coordinate of the reposition image [mm]; z : z-coordinate [mm]; z_{ref} : z-coordinate of the reference image [mm]; z_{rep} : z-coordinate of the reposition image [mm]; ϕ_{abs} : Reposition misorientation angle [°]

Declarations

Conflict of Interest The authors have no relevant financial of non-financial interests to disclose.

References

1. Zhao J, Sang Y, Duan F (2019) The state of the art of two-dimensional digital image correlation computational method. Eng Rep 1. https://doi.org/10.1002/eng2.12038
2. Chu TC, Ranson WF, Sutton MA (1985) Applications of digital-image-correlation techniques to experimental mechanics. Exp Mech 25:232–244. https://doi.org/10.1007/BF02325092
3. Casperson MC, Carroll JD, Lambros J et al (2014) Investigation of thermal effects on fatigue crack closure using multiscale digital image correlation experiments. Int J Fatigue 61:10–20. https://doi.org/10.1016/j.ijfatigue.2013.11.020
4. Tong J, Alshammrei S, Wigger T et al (2018) Full-field characterization of a fatigue crack: Crack closure revisited. Fatigue Fract Eng Mater Struct. https://doi.org/10.1111/ffe.12769
5. Tong J, Alshammrei S, Lin B et al (2019) Fatigue crack closure: A myth or a misconception? Fatigue Fract Eng Mater Struct 42:2747–2763. https://doi.org/10.1111/ffe.13112
6. Vasco-Olmo JM, Díaz Garrido FA, Antunes FV et al (2020) Plastic CTOD as fatigue crack growth characterising parameter in 2024–T3 and 7050–T6 aluminium alloys using DIC. Fatigue Fract Eng Mater Struct 43:1719–1730. https://doi.org/10.1111/ffe.13210
7. Carroll JD, Abuzaid W, Lambros J et al (2013) High resolution digital image correlation measurements of strain accumulation in fatigue crack growth. Int J Fatigue 57:140–150. https://doi.org/10.1016/j.ijfatigue.2012.06.010
8. Lu Y-W, Lupton C, Zhu M-L et al (2015) In Situ Experimental Study of Near-Tip Strain Evolution of Fatigue Cracks. Exp Mech 55:1175–1185. https://doi.org/10.1007/s11340-015-0014-4
9. Tong J, Lin B, Lu Y-W et al (2015) Near-tip strain evolution under cyclic loading: In situ experimental observation and numerical modelling. Int J Fatigue 71:45–52. https://doi.org/10.1016/j.ijfatigue.2014.02.013
10. Vasco-Olmo JM, Díaz FA, García-Collado A et al (2015) Experimental evaluation of crack shielding during fatigue crack growth using digital image correlation. Fatigue Fract Engng Mater Struct 38:223–237. https://doi.org/10.1111/ffe.12136
11. Vasco-Olmo JM, James MN, Christopher CJ et al (2016) Assessment of crack tip plastic zone size and shape and its influence on crack tip shielding. Fatigue Fract Engng Mater Struct 39:969–981. https://doi.org/10.1111/ffe.12436
12. Duan QY, Li JQ, Li YY et al (2020) A novel parameter to evaluate fatigue crack closure: Crack opening ratio. Int J Fatigue 141:105859. https://doi.org/10.1016/j.ijfatigue.2020.105859
13. Réthoré J (2015) Automatic crack tip detection and stress intensity factors estimation of curved cracks from digital images. Int J Numer Meth Engng 103:516–534. https://doi.org/10.1002/nme.4905
14. Strohmann T, Starostin-Penner D, Breitbarth E et al (2021) Automatic detection of fatigue crack paths using digital image correlation and convolutional neural networks. Fatigue Fract Eng Mater Struct 44:1336–1348. https://doi.org/10.1111/ffe.13433
15. Melching D, Strohmann T, Requena G et al (2022) Explainable machine learning for precise fatigue crack tip detection. Sci Rep 12:9513. https://doi.org/10.1038/s41598-022-13275-1
16. Bouaziz MA, Marae-Djouda J, Zouaoui M et al (2021) Crack growth measurement and J -integral evaluation of additively manufactured polymer using digital image correlation and FE modeling. Fatigue Fract Eng Mater Struct 44:1318–1335. https://doi.org/10.1111/ffe.13431
17. Molteno MR, Becker TH (2015) Mode I-III Decomposition of the J -integral from DIC Displacement Data. Strain 51:492–503. https://doi.org/10.1111/str.12166
18. Breitbarth E, Strohmann T, Besel M et al (2019) Determination of Stress Intensity Factors and J integral based on Digital Image Correlation. Frattura ed Integrità Strutturale 13:12–25. https://doi.org/10.3221/IGF-ESIS.49.02
19. Rthor J, Gravouil A, Morestin F et al (2005) Estimation of mixed-mode stress intensity factors using digital image correlation and an interaction integral. Int J Fract 132:65–79. https://doi.org/10.1007/s10704-004-8141-4
20. Yoneyama S, Morimoto Y, Takashi M (2006) Automatic evaluation of mixed-mode stress intensity factors utilizing digital image correlation. Strain 42:21–29. https://doi.org/10.1111/j.1475-1305.2006.00246.x
21. Christopher CJ, James MN, Patterson EA et al (2007) Towards a new model of crack tip stress fields. Int J Fract 148:361–371. https://doi.org/10.1007/s10704-008-9209-3

22. Besel M, Breitbarth E (2016) Advanced analysis of crack tip plastic zone under cyclic loading. Int J Fatigue 93:92–108. https://doi.org/10.1016/j.ijfatigue.2016.08.013

23. Breitbarth E, Besel M (2017) Energy based analysis of crack tip plastic zone of AA2024-T3 under cyclic loading. Int J Fatigue 100:263–273. https://doi.org/10.1016/j.ijfatigue.2017.03.029

24. Durmaz AR, Hadzic N, Straub T et al (2021) Efficient Experimental and Data-Centered Workflow for Microstructure-Based Fatigue Data. Exp Mech 61:1489–1502. https://doi.org/10.1007/s11340-021-00758-x

25. Scheffler M, Aeschlimann M, Albrecht M et al (2022) FAIR data enabling new horizons for materials research. Nature 604:635–642. https://doi.org/10.1038/s41586-022-04501-x

26. Liang Z, Zhang J, Qiu L et al (2021) Studies on deformation measurement with non-fixed camera using digital image correlation method. Measurement 167:108139. https://doi.org/10.1016/j.measurement.2020.108139

27. Qian W, Li J, Zhu J et al (2020) Distortion correction of a microscopy lens system for deformation measurements based on speckle pattern and grating. Optics Lasers Eng 124:105804. https://doi.org/10.1016/j.optlaseng.2019.105804

28. Crammond G, Boyd SW, Dulieu-Barton JM (2013) Speckle pattern quality assessment for digital image correlation. Opt Lasers Eng 51:1368–1378. https://doi.org/10.1016/j.optlaseng.2013.03.014

29. Lecompte D, Smits A, Bossuyt S et al (2006) Quality assessment of speckle patterns for digital image correlation. Opt Lasers Eng 44:1132–1145. https://doi.org/10.1016/j.optlaseng.2005.10.004

30. Liu X-Y, Li R-L, Zhao H-W et al (2015) Quality assessment of speckle patterns for digital image correlation by Shannon entropy. Optik 126:4206–4211. https://doi.org/10.1016/j.ijleo.2015.08.034

31. Dong YL, Pan B (2017) A Review of Speckle Pattern Fabrication and Assessment for Digital Image Correlation. Exp Mech 57:1161–1181. https://doi.org/10.1007/s11340-017-0283-1

32. Pan B, Yu L, Wu D et al (2013) Systematic errors in two-dimensional digital image correlation due to lens distortion. Opt Lasers Eng 51:140–147. https://doi.org/10.1016/j.optlaseng.2012.08.012

33. Dufour J-E, Hild F, Roux S (2014) Integrated digital image correlation for the evaluation and correction of optical distortions. Opt Lasers Eng 56:121–133. https://doi.org/10.1016/j.optlaseng.2013.12.015

34. Zappa E, Mazzoleni P, Matinmanesh A (2014) Uncertainty assessment of digital image correlation method in dynamic applications. Opt Lasers Eng 56:140–151. https://doi.org/10.1016/j.optlaseng.2013.12.016

35. Sutton MA, Yan JH, Tiwari V et al (2008) The effect of out-of-plane motion on 2D and 3D digital image correlation measurements. Opt Lasers Eng 46:746–757. https://doi.org/10.1016/j.optlaseng.2008.05.005

36. Hoult NA, Andy Take W, Lee C et al (2013) Experimental accuracy of two dimensional strain measurements using Digital Image Correlation. Eng Struct 46:718–726. https://doi.org/10.1016/j.engstruct.2012.08.018

37. Haddadi H, Belhabib S (2008) Use of rigid-body motion for the investigation and estimation of the measurement errors related to digital image correlation technique. Opt Lasers Eng 46:185–196. https://doi.org/10.1016/j.optlaseng.2007.05.008

38. Zhang J, Jin G, Ma S et al (2003) Application of an improved subpixel registration algorithm on digital speckle correlation measurement. Opt Laser Technol 35:533–542. https://doi.org/10.1016/S0030-3992(03)00069-0

39. Pan B (2018) Digital image correlation for surface deformation measurement: historical developments, recent advances and future goals. Meas Sci Technol 29:82001. https://doi.org/10.1088/1361-6501/aac55b

40. ASTM Standard Test Method for Measurement of Fatigue Crack Growth Rates 5(E647):1863–1866

41. Paysan F, Breitbarth E (2022) Towards three dimensional aspects of plasticity-induced crack closure: A finite element simulation. Int J Fatigue 163:107092. https://doi.org/10.1016/j.ijfatigue.2022.107092